TURBULENCE MODELLING STUDIES OF SHOCK-WAVE/BOUNDARY-LAYER INTERACTIONS ON HIFiRE-1 AXISYMMETRIC CONE CYLINDER FLARE IN HYPERSONIC FLOWS

Romie Oktovianus Bura [1,2], Fatwa A. Maulana [1]

[1] Faculty of Mechanical and Aerospace Engineering, Bandung Institute of Technology, Bandung 40132, Indonesia.
[2] Faculty of Defense Technology, Republic of Indonesia Defense University, Central Jakarta 10430, Indonesia.

Abstract

In this present work, the turbulent Shock-Wave/Boundary-Layer Interactions (SWBLIs) over a geometry model of HIFiRE-1 axisymmetric cone cylinder flare with a ramp angle of 7 and 33 degrees were analyzed. The condition of dry air at Mach 7.16 on the hypersonic regime was modeled as a perfect gas. A $k - \omega$ turbulence model was used with grid-independence study. Structured quadrilateral blocking was used to perform the computation domain and the simulations presented critical characteristics in SWBLIS, such as wall pressure distribution, wall shear stress distribution and wall heat flux. The simulation results were compared to the experimental result of HIFiRE-1 ground test studies.

Keywords:, SWBLIs, HIFiRE-1, Hypersonic, Turbulence Model, Validation

1. Introduction

Maintained flight at hypersonic speeds presents a persevering challenge to vigorous aerospace vehicle design. Transition to turbulence, large heat transfer rates, high-temperature gas chemistry effects, and shock-wave/boundary-layer interactions (SWBLIs) are among the many issues having particular importance in high-speed level flight that is still poorly understood [1]. At hypersonic speed, the aerothermal conditions are very extreme which can impact the surface pressure load and heating of a vehicle [2]. The SWBLIs cause heating which generates on the body such as on the leading edge of the wing which is responsible for system failure [3]. Besides, an extraordinary aerothermal environment acting on a geometrically thin aerospace vehicle structure can result in noteworthy auxiliary deformations of the vehicle or its control surfaces. The intersection of competing requirements can also result in a situation where fluid-thermal-structure interaction (FTSI) phenomenon and impacts are critical. Moreover, the surface temperature distribution which results from aerothermal loading can change both the mechanical response and the aerodynamics properties of the vehicle in flight. The shock-dominated flows typical of hypersonic flight can show interference effects and shock impingement that increments surface heat transfer rates extraordinarily [4, 5]. Thus, the design configuration of such a vehicle should be under acceptable consideration.

SWBLIs also may lead to boundary layer separation, enhancing heating load, or even turbulent reattachment. A typical schematic diagram for ramp-induced SWBLIs is shown in Figure 1. In the presence of the ramp, the flow becomes deflected abruptly by the compression corner which the adverse pressure gradient leads to the generation of oblique shock waves emanating from the compression corner which interacts with the boundary layer over the wall. Hence, the boundary layer experiences an adverse pressure gradient near the region of the flow deceleration or oblique shock. If the deflection angle is higher than the incipient separation angle, the boundary layer separation takes place well ahead of the compression corner and separation shock forms ahead of the separation region due to the coalescence of compression waves induced by the separation process. The nearly

constant plateau pressure region downstream of the separation point is invariantly considered as the indicator to identify the separation bubble. This recirculation zone extends up to the reattachment point, where the flow re-attaches on the ramp surface [6]. The peak heat-flux rate near the reattachment point (or boundary layer neck) may be much larger than that of elsewhere. In general, the peak heating on a compression ramp may be determined by the state of the separated flow as it re-attaches to the ramp surface [7, 8]. However, the detail of this process may vary depending on the case and if it is examined in a different instant [9].
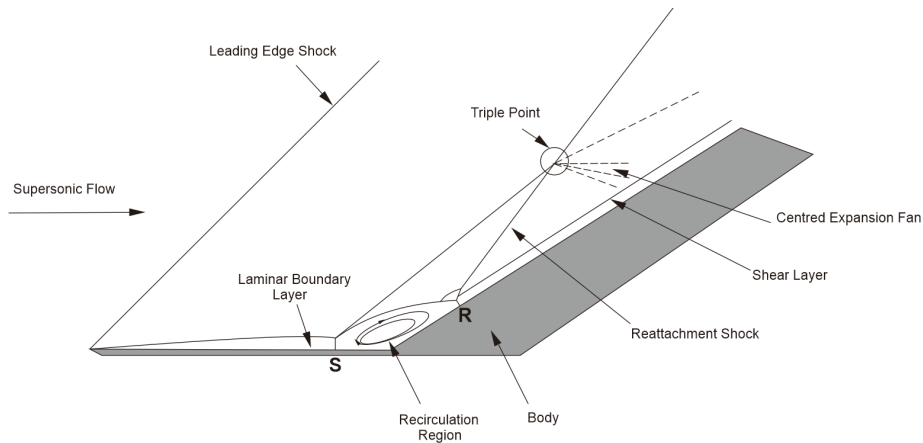

Figure 1 - SWBLIs in compression ramp

The turbulence modeling and the prediction of transition from laminar to turbulent flow is one of the keys to predicting the pressure and heating load which impacts on vehicle body [10]. The state of art turbulence simulations in engineering applications are mainly solving the RANS equations. The associated turbulence modeling remains a major source of uncertainty in the computational prediction of aerodynamic forces and heating for hypersonic vehicles. Typically, turbulence models have been developed for incompressible flows and extended without much change to compressible flows which are responsible for increasing the uncertainties for SWBLIs phenomena in hypersonic flows [7]. In the present study, the pressure and heating load on the HIFiRE-1 vehicle as well as other important phenomena such as point of separation and Mach number distribution were compared by various turbulence models to the experimental data published [11-13]. The ground test of HIFiRE-1 experiments has been developed in the LENS-1 to study the full-scale flight vehicle at selected conditions along the test flight trajectory which in the future can be used to design the next-generation hypersonic vehicle [14]. The schematic diagram of the HIFiRE-1 body is shown in Figure 2.
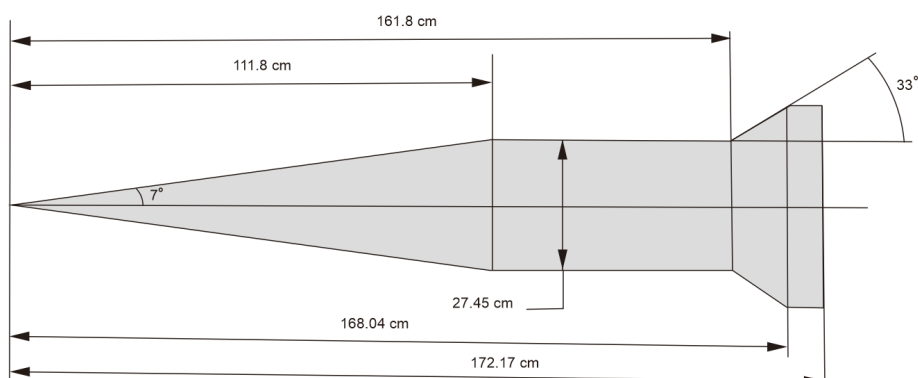

Figure 2 - HIFiRE model dimension

Some related works correspondence in hypersonic flows over a ramp are the study of the surface pressure and heat flux in hypersonic laminar interactions with real gas effects by Hao et al. [15], the effect of leading-edge bluntness toward separation bubble size, boundary layer edge Mach number and temperature, sonic height, boundary layer thickness, skin friction coefficient and pressure by John et al. [16], the studies of unsteady behavior of interaction from hypersonic and air with its thermochemical non-equilibrium effects [17-20], the study of shock wave unsteadiness in SWBLI over compression ramp by Sun et al. [21], 3D model simulation for compression ramp studied by Oliver et al [22] and 3D cone with a control surface studied by Pandey et al. [23], the experimental study of cone-flare with different blunt radius, Stanton number, flare angle, Reynolds number by Carson [24]. Some works were done to improve the numerical accuracy derived from the original turbulence model in hypersonic flow, such as the introduction of SUQ SST by Raje et al. [25], which showed that the improved model could match the experiment value better than the original Menter SST model. The present studies are a part of fundamental research of SWBLIs in hypersonic flows for better experimental and numerical integration, by using existing experimental results as the basis for numerical predictions, in this case is turbulence modelling, with the aim to develop strategies for efficient numerical methods. The present studies also aim to compare several turbulence models with experimental results of HIFiRE-1 and based on our knowledge, the comparison between five turbulence models of $k - \omega$, Spalart Allmaras, Transition SST, $k - \varepsilon$, $k - \omega$, and Reynolds stress for the SWBLI study in the HIFiRE-1 vehicle model has never been performed. In this paper, the result of $k - \omega$ turbulence model is presented.

2. Materials and Methods

The 3D model of fluid domain around the HIFiRE-1 body was modeled as a 2D structured quadrilateral mesh. The 2D quad mesh was then computed as axisymmetric in the solver to mimic the flow in a real 3D model. The computational domain taken in this simulation is the upper portion above the HIFiRE-1 surface. Figure 3 shows the fluid domain and its boundary condition assigned on each side of the domain. Figure 4 shows that 26 blocks were made in this domain to ensure that all-important physics flows could be captured and the refinement was given on the wall surface and the junction between leading-edge, cone-cylinder, cylinder-flare, and flare-aft. To catch important physical flow near the wall, the value of y+ was adjusted close to 1. The mesh element size for each blocking was also adjusted by creating bunching along the edges, which separated among the blocks as such that the relative mesh size in the edge of each block was close to the mesh size in the neighboring block. The result of this mesh size adjustment is shown in Figure 5.
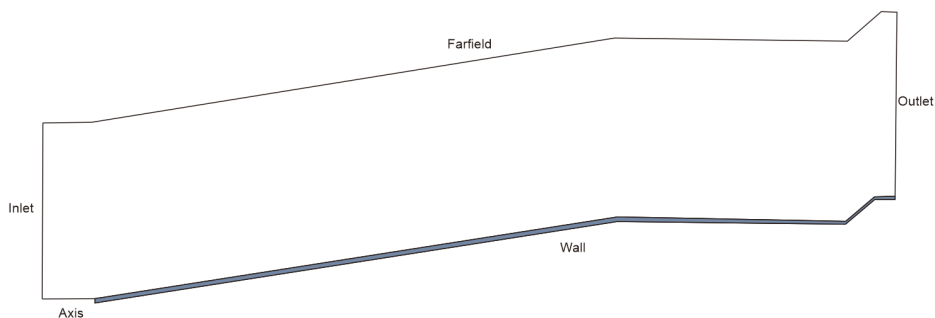

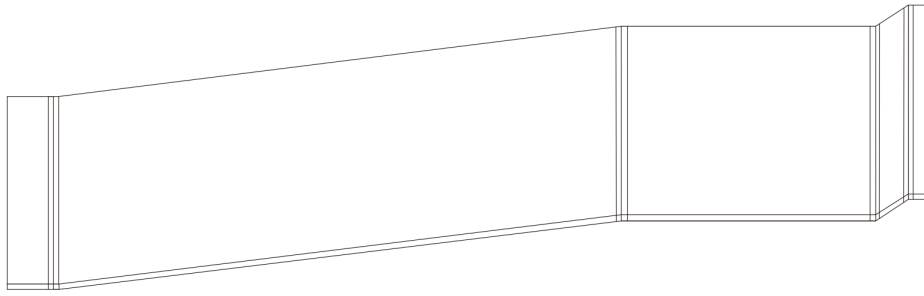Figure 3 - Boundary condition on fluid domain
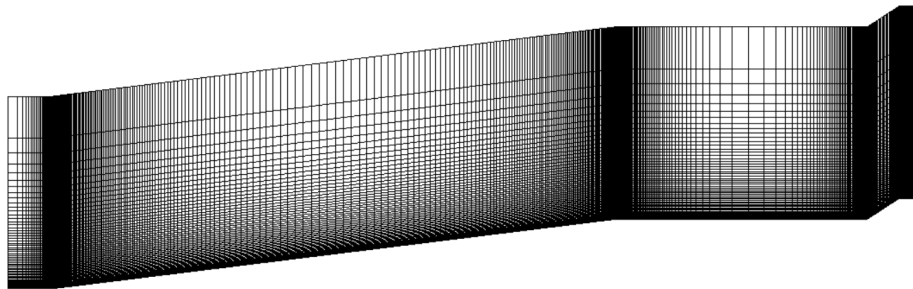
Figure 4 - Fluid domain blocking

Figure 5 - Fluid domain meshing (using 161,728 grid)

The inlet and far-field were assigned as pressure-inlet, the outlet was assigned as pressure-outlet, the wall assigned with no-slip wall and isothermal with determined temperature, and the symmetry as an axis. The assigned boundary condition of the inlet, outlet, wall, far-field, and symmetry have input values as in Table 1 below.

Table 1. Boundary Condition Values

	Inlet	Outlet	Wall	Farfield	Axis
Pressure (Pa)	4728.43	4728.43	-	4728.43	-
Mach Number	7.16	-	-	7.16	-
Temperature (K)	-	-	291.4	-	-

The solver was set up to the density-based setting due to the concern of the air compressibility effect in hypersonic flows [10]. The fluid is assumed to be an ideal gas for present studies, the coefficient of dynamic viscosity (μ) is calculated by making use of Sutherland's law [26]. The solution methods formulation was chosen to be implicit with the flux type Roe-FDS. The spatial discretization gradient was chosen to Green-Gauss Node Element and the modified turbulent viscosity to be first-order upwind and the transient formulation to be second-order implicit. The control of the solver such as the CFL number was set to be 5 and the under-relaxation factor was set to be default. The simulation conducted using transient analysis as the main flow features, such as the entire laminar separated region, the strong bow-shock, the triple point and the location of the separation shock show an unsteady [27] and time-dependent behaviour [28]. The study about computational test time on double compression hypersonic flow with averaged data from timestep 150 μs to 310 μs by Durna et al. [29] and another experimental study by Swantek et al. [30] reveal that the steady flows in double wedges occur at 327 μs, which then assessed by Badr et al. [4] resulting in unsteady flows after 327 μs in numerical simulation. Hence, in our case the simulation was carried out from 0 μs to 15 ms, by 0.5 μs timestep, to ensure convergence. After running the simulation, the adapted mesh feature was used to refine the mesh size in the area where the pressure gradient value was large, i.e., in the vicinity of the shock wave. The equation for $k - \omega$ turbulence modeling in this present work can be stated as below [31],

4

$$\frac{\partial}{\partial t}(\rho k) + \frac{\partial}{\partial x_i}(\rho k u_i) = \frac{\partial}{\partial x_j}\left(\Gamma_k \frac{\partial k}{\partial x_j}\right) + G_k - Y_k + S_k \tag{1}$$

$$\frac{\partial}{\partial t}(\rho \omega) + \frac{\partial}{\partial x_i}(\rho \omega u_i) = \frac{\partial}{\partial x_j}\left(\Gamma_\omega \frac{\partial \omega}{\partial x_j}\right) + G_\omega - Y_\omega + S_\omega \tag{2}$$

Where k is the turbulence kinetic energy, ω is the specific dissipation rate, G_k is the generation of turbulence kinetic energy due to mean velocity gradients, G_ω is the generation of ω. Γ_k and Γ_ω are the effective diffusivity of k and ω respectively, S_k and S_ω are user-defined source terms.

3. Results and Discussion
3.1 Steady-State Condition and Grid Independence Test
Difference turbulence modelling yields various instability during running the simulation. As a result, some turbulence modelling cannot converge at given low residual criteria. In this case, the grid independence test was conducted using the $k - \omega$ turbulence model with a 0.01 residual criteria value. A residual for the density-based solver is simply the time rate of change of the conserved variable (W). The RMS residual is the square root of the average of the squares of the residuals in each cell of the domain

$$R\left(W\right) = \sqrt{\sum \left(\frac{\partial W}{\partial t}\right)^2} \tag{3}$$

In general, it is difficult to judge convergence by examining the residuals defined in equation (1) since no scaling is employed. Hence in the present studies, the globally scaled residual is used, which defined as

$$\frac{R\left(W\right)_{iteration\ N}}{R\left(W\right)_{iteration\ 5}} \tag{4}$$

The denominator is the largest absolute value of the residual in the first five iterations. The convergence criterion was set to absolute (if the scaled residual is less than the user-specified value, that equation is deemed to have converged for a timestep). The L∞ norm takes the maximum residual value for each grid without dividing the maximum residual to the previous maximum first five iterations, which differ from the globally scaled residual definition explained before. The value of globally scaled residual was set to 0.01. There is no real precursor to determine what residual error values should be reduced to for acceptable convergence. This is because residual error may also reflect local areas of instability which is not representative of global convergence. Hence the simulations were also carried by monitoring some quantitative result of interest such as the bubble separation length and wall heat flux.

Some flow features such as wall surface friction, shock wave location, separation and reattachment are mostly concerned in the research work of turbulent SWBLIs [32]. In this work, flow separation and the appearance of excessive heat on the wall surface were essential parameters to be examined. The grid elements will be studied by varying the number of the elements in the x-direction, y-direction, and both x-y directions denoted by grid independence test 1, 2, and 3 respectively. The grid independence test is examined started from 266 x 304 grid elements as baseline, which then increased by 50% in x-direction, y-direction, and both x-y directions. The value of separation point (x_s), reattachment point (x_r), and bubble separation length (x_{bsl}) are monitored for every 5 ms for steady state condition test.

For comparison, the simulation using steady solver was also given. For the steady simulation, the implicit solver is used with the Roe-FDS flux type. The spatial discretization was using Least Square Cell-Based. The flow, the turbulent kinetic energy, and the specific dissipation rate was using the first order upwind. The Convergence Acceleration for Stretched Mesh and High Order Term Relaxation was turned on with 0.05 value of under relaxation for all variables. In solution control, the CFL number was set to 0.05 and the positivity rate limit was set to 0.05. Standard initialization was used with the far field as reference and FMG initialization also applied after. The first order to higher order blending factor was set to 0.75. The results for varying the elements number in x direction are tabulated in Table 2.

Table 2. Steady-state condition and grid independence Test 1

N_X	N_y	N	t (ms)	x_s (m)	x_r (m)	x_{bsl} (m)
				Steady State Condition and Grid Independence Test 1 (Mesh variation in x-direction)		
266	304	80864	5 ms	1.60784	1.6227	0.01486
			10 ms	1.60949	1.62194	0.01245
			15 ms	1.61001	1.62168	0.01168
			20 ms	1.61058	1.62157	0.01099
			25 ms	1.61062	1.62153	0.01091
			30 ms	1.61063	1.62152	0.01088
			steady	1.6097	1.6215	0.0107
399	304	121296	5 ms	1.6083	1.62261	0.01431
			10 ms	1.60964	1.62208	0.01244
			15 ms	1.61009	1.62185	0.01176
			20 ms	1.61025	1.62176	0.01151
			25 ms	1.61052	1.62172	0.01121
			30 ms	1.61053	1.62171	0.01118
			steady	1.5979	1.625	0.0111
532	304	161728	5 ms	1.60915	1.62229	0.01315
			10 ms	1.60991	1.62195	0.01204
			15 ms	1.61019	1.62181	0.01163
			20 ms	1.61029	1.62177	0.01147
			25 ms	1.61034	1.62174	0.0114
			30 ms	1.61049	1.62173	0.01124
			steady	1.5972	1.6253	0.0112
665	304	202160	5 ms	1.60889	1.62238	0.01349
			10 ms	1.60942	1.62218	0.01276
			15 ms	1.60976	1.62202	0.01227
			20 ms	1.61002	1.62191	0.01189
			25 ms	1.61016	1.62185	0.01169
			30 ms	1.61022	1.62182	0.0116
			steady	1.6	1.6251	0.0115
798	304	242592	5 ms	1.6083	1.62264	0.01434
			10 ms	1.60908	1.62233	0.01324
			15 ms	1.60971	1.62206	0.01236
			20 ms	1.60994	1.62194	0.012
			25 ms	1.61007	1.6219	0.01183
			30 ms	1.6101	1.62188	0.01178
			steady	1.5826	1.6295	0.0117

The results for varying the number of elements in the y-direction are tabulated in Table 3.

Table 3. Steady-state condition and grid independence Test 2

Steady State Condition and Grid Independence Test 2 (Mesh variation in y-direction)						
N_X	N_y	N	t (ms)	x_s (m)	x_r (m)	x_{bsl} (m)
266	304	80864	5 ms	1.60784	1.6227	0.01486
			10 ms	1.60949	1.62194	0.01245
			15 ms	1.61001	1.62168	0.01168
			20 ms	1.61058	1.62157	0.01099
			25 ms	1.61062	1.62153	0.01091
			30 ms	1.61063	1.62152	0.01088
			steady	1.6097	1.6215	0.0107
266	456	121296	5 ms	1.60946	1.62206	0.0126
			10 ms	1.6093	1.62209	0.01279
			15 ms	1.60942	1.62196	0.01254
			20 ms	1.60957	1.62194	0.01237
			25 ms	1.60967	1.6219	0.01222
			30 ms	1.60976	1.62186	0.01209
			steady	1.6094	1.6217	0.011
266	608	161728	5 ms	1.60996	1.62185	0.01189
			10 ms	1.6093	1.62214	0.01284
			15 ms	1.60924	1.62218	0.01294
			20 ms	1.60924	1.62217	0.01293
			25 ms	1.60925	1.62216	0.0129
			30 ms	1.60927	1.62214	0.01288
			steady	1.6087	1.6221	0.012
266	760	202160	5 ms	1.61088	1.62162	0.01074
			10 ms	1.60957	1.62203	0.01246
			15 ms	1.60928	1.62216	0.01289
			20 ms	1.60921	1.62222	0.01301
			25 ms	1.60919	1.62224	0.01305
			30 ms	1.60918	1.62224	0.01306
			steady	1.6087	1.6221	0.0124
266	912	242592	5 ms	1.61352	1.61951	0.00599
			10 ms	1.61142	1.62165	0.01023
			15 ms	1.6092	1.62245	0.01325
			20 ms	1.6082	1.62263	0.01443
			25 ms	1.60806	1.62276	0.0147
			30 ms	1.60794	1.62283	0.01489
			95 ms	1.60919	1.62211	0.01293
			steady	1.6098	1.6218	0.0123

The results for varying the number of the elements in the x and y direction are tabulated in Table 4.

Table 4. Steady-state condition and grid independence Test 3

N_X	N_y	N	t (ms)	x_s (m)	x_r (m)	x_{bsl} (m)
				Steady State Condition and Grid Independence Test 3 (Mesh variation in x-y direction)		
266	304	80864	5 ms	1.60784	1.6227	0.01486
			10 ms	1.60949	1.62194	0.01245
			15 ms	1.61001	1.62168	0.01168
			20 ms	1.61058	1.62157	0.01099
			25 ms	1.61062	1.62153	0.01091
			30 ms	1.61063	1.62152	0.01088
			steady	1.6102	1.6214	0.0107
399	456	181944	5 ms	1.60778	1.62296	0.01519
			10 ms	1.60781	1.62288	0.01507
			15 ms	1.60828	1.6226	0.01432
			20 ms	1.60878	1.62239	0.01361
			25 ms	1.60908	1.62223	0.01315
			30 ms	1.60927	1.62215	0.01289
			60 ms	1.60979	1.62194	0.01215
			steady	1.6001	1.625	0.0119
532	608	323456	5 ms	1.60931	1.62221	0.0129
			10 ms	1.6085	1.62269	0.01419
			15 ms	1.60824	1.62276	0.01452
			20 ms	1.60831	1.6227	0.01438
			25 ms	1.60853	1.62263	0.0141
			30 ms	1.60866	1.62257	0.01391
			60 ms	1.60914	1.62241	0.01328
			steady	1.5939	1.6287	0.0129
665	760	505400	5 ms	1.61025	1.62211	0.01186
			10 ms	1.60911	1.6223	0.01319
			15 ms	1.60893	1.62237	0.01344
			20 ms	1.60889	1.62241	0.01352
			25 ms	1.60875	1.62244	0.01369
			30 ms	1.60873	1.62245	0.01372
			steady	1.598	1.6301	0.0134
798	912	727776	5 ms	1.60887	1.62241	0.01354
			10 ms	1.60767	1.62344	0.01576
			15 ms	1.60686	1.62323	0.01637
			20 ms	1.607	1.62323	0.01623
			25 ms	1.60715	1.62322	0.01607
			30 ms	1.60715	1.6232	0.01605
			steady	1.5961	1.6307	0.0135

3.2 Result and Discussion

The bubble separation length data from Table 2, Table 3, and Table 4 are plotted in Figure 6, Figure 7, and Figure 8 respectively. From those Figures, we can see the differences in bubble separation length for each grid element value with respect to the time evolved during simulation, particularly Figure 6 and 8. The differences are less for Figure 7. For the time steps of 5 ms, 10 ms, 15 ms, and 20 ms, the value of bubble separation length differs too much. Hence, we can conclude the steady state has not been achieved. The difference in bubble separation length for 25 ms, 30 ms and later is less than 5% for each grid elements value.
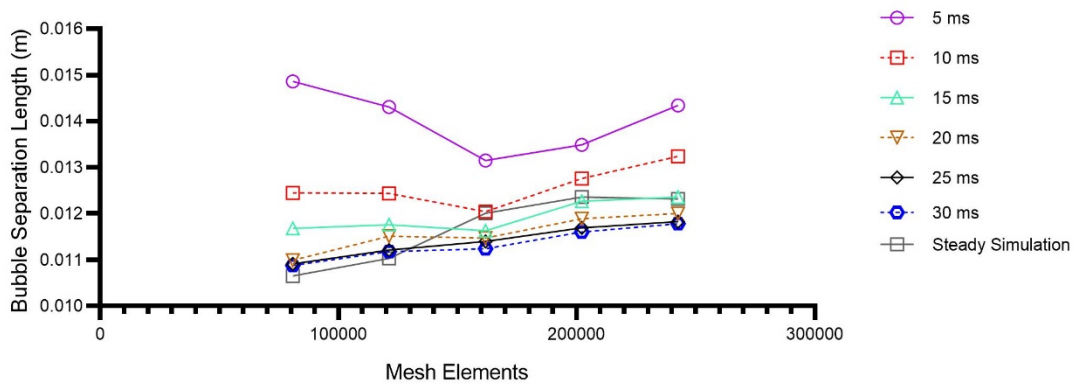

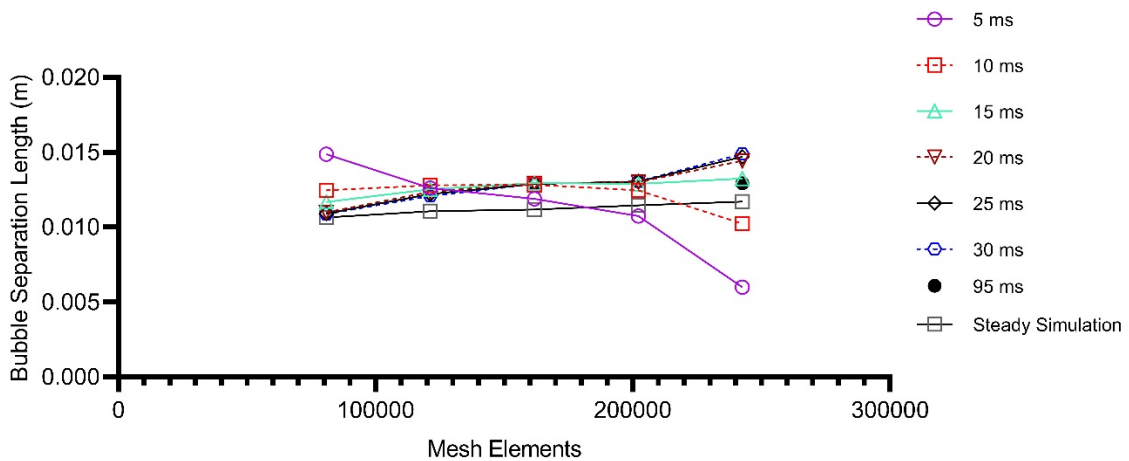Figure 6 - Steady-state condition and grid independence Test 1

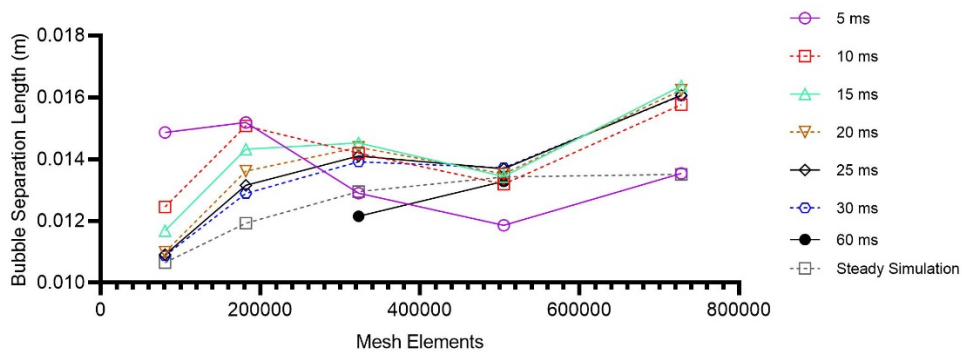Figure 7 - Steady-state condition and grid independence Test 2

Figure 8 - Steady-state condition and grid independence Test 3

9

Some fluctuations in Figure 8 are due to the sampling point taken for wall shear stress by the code limited by the input grid number being interpolated to find the separation and reattachment locations, which are denoted by the zero value of wall shear stress. This interpolation process may cause small inaccuracies in the determination of bubble separation length. Hence, another parameter by considering the wall heat flux value was carried out for the grid independence study. Of interest are the grids in 798 x 304, 266 x 912, 399 x 456, and 532 x 608 (each representing changes in x-direction, y-direction, and both x-y directions, with 266 x 304 grid elements as baseline). Table 5, 6, 7, and 8 shows the maximum wall heat flux location, maximum wall heat flux value, and difference to the experiment data for every simulation time $\Delta t = 2.5$ ms.

Table 5. Max wall heat flux differences to experiment result for 266 x 304 grid

Nx	Ny	N	t	Max Wall Heat Flux Location (m)	Max Wall Heat Flux (Q/cm^2)	Difference w.r.t experiment (%)
			Experiment	1.667	376.84	0
			2.5 ms	1.67951	244.464	35.13
			5 ms	1.67951	274.951	27.04
			7.5 ms	1.67951	285.048	24.36
			10 ms	1.67951	287.509	23.71
			12.5 ms	1.67951	287.538	23.7
798	304	242592	15 ms	1.67951	287.32	23.76
			17.5 ms	1.67951	287.194	23.79
			20 ms	1.67983	291.497	22.65
			22.5 ms	1.67951	287.041	23.83
			25 ms	1.67951	287.041	23.83
			27.5 ms	1.67951	286.95	23.85
			30 ms	1.67951	286.928	23.86

Table 6. Max wall heat flux differences to experiment result for 798 x 304 grid

Nx	Ny	N	t	Max Wall Heat Flux Location (m)	Max Wall Heat Flux (Q/cm^2)	Difference w.r.t experiment (%)
			Experiment	1.667	376.84	0
			2.5 ms	1.67999	260.046	30.99
			5 ms	1.67999	292.447	22.39
			7.5 ms	1.67999	302.048	19.85
			10 ms	1.67999	304.161	19.29
			12.5 ms	1.67999	304.308	19.25
798	304	242592	15 ms	1.67999	304.003	19.33
			17.5 ms	1.67999	303.69	19.41
			20 ms	1.67999	303.348	19.5
			22.5 ms	1.67999	303.17	19.55
			25 ms	1.67999	303.07	19.58
			27.5 ms	1.67999	303.024	19.59
			30 ms	1.67999	302.987	19.6

Table 7. Max wall heat flux differences to experiment result for 266 x 912 grid

Nx	Ny	N	t	Max Wall Heat Flux Location (m)	Max Wall Heat Flux (Q/cm^2)	Difference w.r.t experiment (%)
			Experiment	1.667	376.84	0
			2.5 ms	1.6253	162.863	56.78
			5 ms	1.67951	216.737	42.49
			7.5 ms	1.67951	213.798	43.27
			10 ms	1.67951	218.101	42.12
			12.5 ms	1.67951	232.306	38.35
			15 ms	1.67951	241.939	35.8
			17.5 ms	1.67951	248.012	34.19
			20 ms	1.67951	252.434	33.01
			22.5 ms	1.67951	254.964	32.34
			25 ms	1.67951	255.88	32.1
			27.5 ms	1.67951	256.726	31.87
			30 ms	1.67951	257.479	31.67
			32.5 ms	1.67951	259.455	31.15
			35 ms	1.67951	260.93	30.76
			37.5 ms	1.67951	262.635	30.31
			40 ms	1.67951	265.733	29.48
			42.5 ms	1.67951	267.674	28.97
			45 ms	1.67951	269.674	28.44
266	912	242592	47.5 ms	1.67951	271.732	27.89
			50 ms	1.67951	273.499	27.42
			52.5 ms	1.67951	275.675	26.85
			55 ms	1.67951	277.671	26.32
			57.5 ms	1.67951	279.477	25.84
			60 ms	1.67951	281.337	25.34
			62.5 ms	1.67951	283.262	24.83
			65 ms	1.67951	285.004	24.37
			67.5 ms	1.67951	286.424	23.99
			70 ms	1.67951	287.843	23.62
			72.5 ms	1.67951	289.066	23.29
			75 ms	1.67951	290.161	23
			77.5 ms	1.67951	291.118	22.75
			80 ms	1.67951	291.91	22.54
			82.5 ms	1.67951	292.528	22.37
			85 ms	1.67951	292.994	22.25
			87.5 ms	1.67951	293.33	22.16
			90 ms	1.67951	293.552	22.1
			92.5 ms	1.67951	293.631	22.08
			95 ms	1.67951	293.633	22.08

Table 8. Max wall heat flux differences to experiment result for 399 x 456 grid

Nx	Ny	N	t	Max Wall Heat Flux Location (m)	Max Wall Heat Flux (Q/cm^2)	Difference w.r.t experiment (%)
			Experiment	1.667	376.84	0
			2.5 ms	1.67983	256.021	32.06
			5 ms	1.67983	246.857	34.49
			7.5 ms	1.67983	264.129	29.91
			10 ms	1.67983	274.589	27.13
			12.5 ms	1.67983	279.864	25.73
			15 ms	1.67983	286.573	23.95
			17.5 ms	1.67983	289.382	23.21
			20 ms	1.67983	291.497	22.65
			22.5 ms	1.67983	292.621	22.35
			25 ms	1.67983	293.177	22.2
			27.5 ms	1.67983	293.417	22.14
399	456	181944	30 ms	1.67983	293.49	22.12
			32.5 ms	1.67983	293.484	22.12
			35 ms	1.67983	293.445	22.13
			37.5 ms	1.67983	293.397	22.14
			40 ms	1.67983	293.349	22.16
			42.5 ms	1.67983	293.31	22.17
			45 ms	1.67983	293.267	22.18
			47.5 ms	1.67983	293.22	22.19
			50 ms	1.67983	293.188	22.2
			52.5 ms	1.67983	293.161	22.21
			55 ms	1.67983	293.139	22.21
			57.5 ms	1.67983	293.121	22.22
			60 ms	1.67983	293.106	22.22

Table 9. Max wall heat flux differences to experiment result for 532 x 608 grid

Ny	N	t	Max Wall Heat Flux Location (m)	Max Wall Heat Flux (Q/cm^2)	Difference w.r.t experiment (%)
		Experiment	1.667	376.84	0
		2.5 ms	1.67979	266.916	29.17
		5 ms	1.67979	260.705	30.82
		7.5 ms	1.67979	258.663	31.36
		10 ms	1.67979	265.149	29.64
		12.5 ms	1.67979	270.444	28.23
		15 ms	1.67979	276.119	26.73
		17.5 ms	1.67979	279.221	25.9
		20 ms	1.67979	281.913	25.19
		22.5 ms	1.67979	284.1	24.61
		25 ms	1.67979	286.106	24.08
		27.5 ms	1.67979	287.67	23.66
532	608	323456	30 ms	1.67979	290.729	22.85
		32.5 ms	1.67979	291.508	22.64
		35 ms	1.67979	292.268	22.44
		37.5 ms	1.67979	292.867	22.28
		40 ms	1.67979	293.231	22.19
		42.5 ms	1.67979	293.457	22.13
		45 ms	1.67979	293.594	22.09
		47.5 ms	1.67979	293.67	22.07
		50 ms	1.67979	293.711	22.06
		52.5 ms	1.67979	293.723	22.06
		55 ms	1.67979	293.715	22.06
		57.5 ms	1.67979	293.7	22.06
		60 ms	1.67979	293.685	22.07

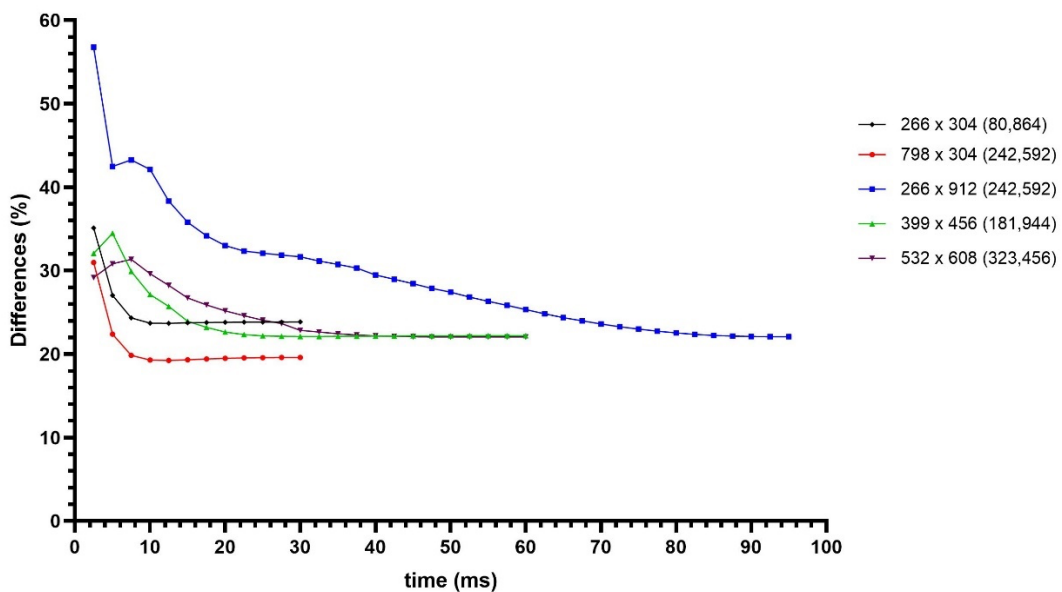The data from Table 5, Table 6, Table 7, Table 8 and Table 9 are presented in Figure 9.

Figure 9 - Wall Heat Flux Comparison for Grid Independence Test

13

Figure 9 shows that increasing grid elements 50% in x-direction, y-direction, and both x-y direction result in smaller differences or closer agreement with experimental results. From Figure 9, it can also be seen that 50% in x-direction increase results in closest agreement with experimental results. That case also has the fastest time to reach steady-state condition, while 50% in y-direction increase required more time than all cases to reach steady-state condition.

The results of the wall heat flux for 4 different grid elements are shown in Figure 10 and compared with the experimental results of HIFiRE-1.
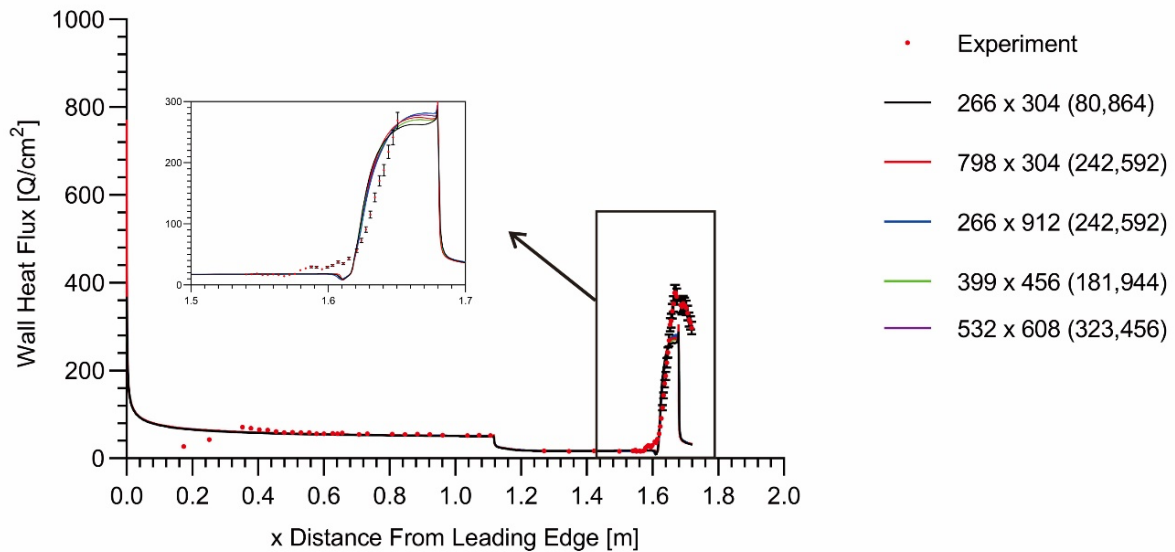
Figure 10 - Wall Heat Flux comparison with experimental results of HIFiRE-1

Figure 10 shows that the maximum wall heat flux occurs in vicinity of the vehicle's nose (near $x = 0$ m). In the present study, the point of interest is the wall heat flux near the compression ramp (cylinder-flare) region. The location of maximum wall heat flux and its corresponding wall heat flux values near the cylinder-flare region are shown in Table 9. The differences with respect to the experiment data are also shown in Table 10.

Table 10. Maximum Wall Heat Flux Locations and Maximum Wall Heat Flux Values

Nx	Ny	N	t (ms)	Max Wall Heat Flux Location (m)	Max Wall Heat Flux (Q/cm^2)	Difference Experiment (%)
		Experiment	-	1.6670	376.84	0
798	304	242,592	30	1.67999	302.987	19.6
266	912	242,592	95	1.67951	293.633	22.08
399	456	181,944	60	1.67983	293.106	22.22
532	608	323,456	60	1.67979	293.685	22.07

In Figure 10, the simulation for 4 grid elements and experimental data with uncertainty from the device was 5% [13] are shown. In Table 10 the closest value of maximum Wall Heat Flux with respect to experiment is the case with 50% in x-direction increase. The comparison for pressure and wall shear stress on the wall surface are shown in Figure 11 and 12 respectively. The experimental values shown in red dot with error bars which caused by the deviation or uncertainty of 3% from the piezoelectric pressure sensor [10], [13].
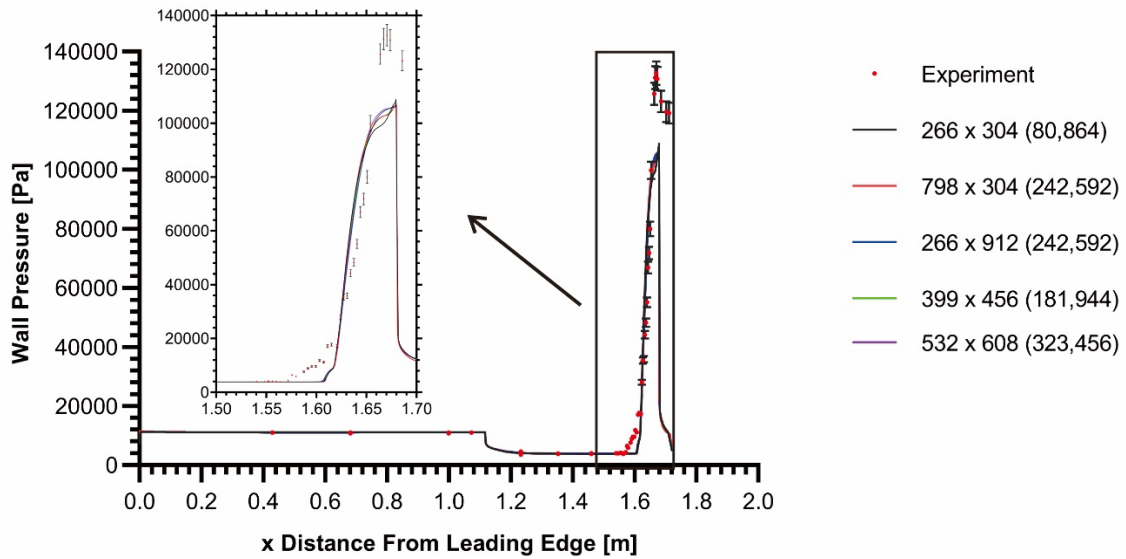
Figure 11 – Wall Pressure comparison with experimental results of HIFiRE-1

The locations of maximum wall pressure and its corresponding wall pressure values are shown in Table 11. The relative differences of value compared to the experiment data are also presented. Table 11 shows that the closest value of Wall Pressure with respect to experiment is the case with 50% in y-direction increase. However, the differences are generally negligible.

Table 11. Maximum Wall Pressure Locations and Maximum Wall Pressure Values

Nx	Ny	N	t (ms)	Max Pressure Location (m)	Max Pressure (Pa)	Difference to Experiment (%)
		Experiment	-	1.6703	132717.2	0
798	304	242,592	30	1.67934	106927	19.43
266	912	242,592	95	1.67951	107428	19.05
399	456	181,944	60	1.67983	107186	19.23
532	608	323,456	60	1.67979	107033	19.35

The wall shear stress on the body surface was plotted in the same manner as the wall pressure distribution plot, except that the experimental value taken was only the point of separation as our main concern. From available data, the point of flow separation is nearly 1.575 m from leading edge [3] which is pictured by red dashed line in Figure 12.
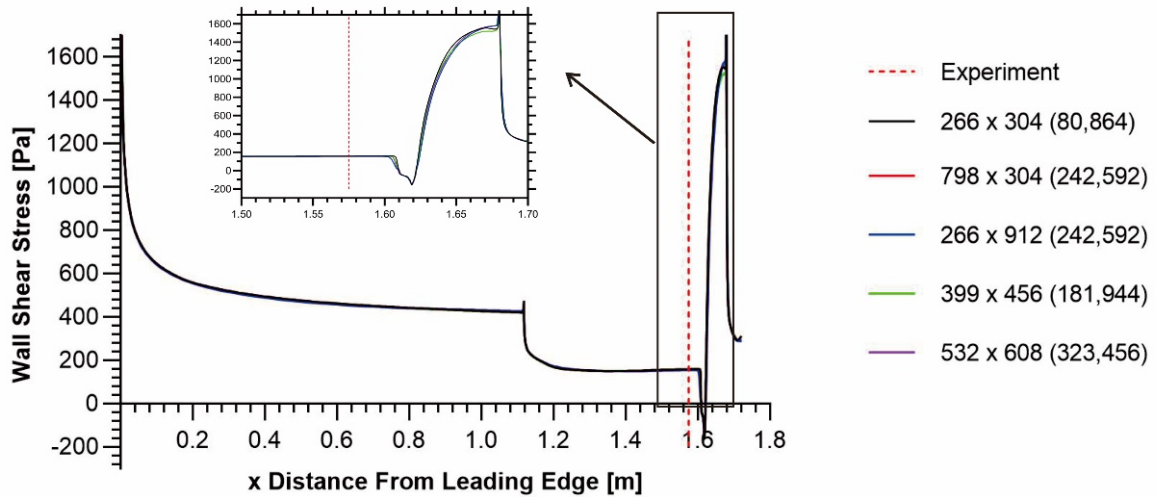
Figure 12 – Wall Shear Stress Comparison

The separation locations are shown in Table 12 with its relative differences with respect to the experimental data. Table 12 shows that the closest value of separation location with respect to experiment is the case with 50% in x-y direction increase. However, the differences are also generally negligible as with the wall pressure results.

Table 12. Separation Locations

Nx	Ny	N	t (ms)	Separation Location (m)	Difference to Experiment (%)
		Experiment	-	~ 1.575	0
798	304	242,592	30	1.6101	2.22857
266	912	242,592	95	1.60918	2.17016
399	456	181,944	60	1.60979	2.20889
532	608	323,456	60	1.60914	2.16762

4. Conclusions

In the present study of hypersonic flow around HIFiRE-1 body axisymmetric cone cylinder flare with a ramp angle of 7 and 33 degrees at Mach 7.16, the steady-state condition of turbulent SWBLIs simulation and grid independence test, using $k - \omega$ turbulence model, have been performed. These results have also been analyzed to compare their accuracy with HIFiRE-1 experimental results. The grid independence test results have shown variations of reaching steady-state condition. The comparisons show that the case with 50% in x-direction increase has the closest agreement of maximum Wall Heat Flux with experimental result. While the closest value of maximum Wall Pressure with respect to experiment is the case with 50% in y-direction increase. However, the differences of Wall Pressure are generally negligible. Interestingly, the closest value of separation location with respect to experiment is the case with 50% in x-y direction increase. These results of grid independence test as well as comparisons with experimental results justify further studies of the turbulence models with, which is expected to reveal the numerical and physical aspects of the predictions of turbulent SWBLIs with aim to develop strategies for efficient numerical methods.

5. Data Availability

The data used to support the findings of this study are available from the corresponding author upon request.

6. Conflicts of Interest

The author(s) declare(s) that there is no conflict of interest regarding the publication of this paper.

7. Contact Author Email Address

Correspondence should be addressed to Romie Oktovianus Bura, mailto: romiebura@ae.itb.ac.id, romiebura@idu.ac.id and sbli1@yahoo.com

8. Copyright Statement

The authors confirm that they, and/or their company or organization, hold copyright on all of the original material included in this paper. The authors also confirm that they have obtained permission, from the copyright holder of any third-party material included in this paper, to publish it as part of their paper. The authors confirm that they give permission or have obtained permission from the copyright holder of this paper, for the publication and distribution of this paper as part of the ICAS proceedings or as individual off-prints from the proceedings.

References

[1] R. J. Yentsch and D. V. Gaitonde, "Numerical investigation of hypersonic phenomena encountered in HIFiRE flight 1," *50th AIAA Aerosp. Sci. Meet. Incl. New Horizons Forum Aerosp. Expo.*, no. January, pp. 1–12, 2012, doi: 10.2514/6.2012-943.

[2] A. A. PASHA and K. A. JUHANY, "Numerical simulation of compression corner flows at Mach number 9," *Chinese J. Aeronaut.*, vol. 33, no. 6, pp. 1611–1624, 2020, doi: 10.1016/j.cja.2020.01.005.

[3] M. Holden and M. Maclean, "Experimental Studies of Shock Wave / Turbulent Boundary Layer Interaction in," no. July, pp. 1–23, 2010.

[4] M. A. Badr and D. D. Knight, "Shock Wave Laminar Boundary Layer Interaction over a Double Wedge in a high mach Number Flow," *52nd Aerosp. Sci. Meet.*, no. January, pp. 1–11, 2014, doi: 10.2514/6.2014-1136.

[5] B. T. Sullivan, T. Whalen, S. Laurence, and D. J. Bodony, "Direct simulation of fluid-structure interaction in compression ramp with embedded compliant panel," *AIAA Aviat. 2019 Forum*, no. June, pp. 1–45, 2019, doi: 10.2514/6.2019-3545.

[6] B. John, V. N. Kulkarni, and G. Natarajan, "Shock wave boundary layer interactions in hypersonic flows," *Int. J. Heat Mass Transf.*, vol. 70, pp. 81–90, 2014, doi: 10.1016/j.ijheatmasstransfer.2013.10.072.

[7] G. Tu, X. Deng, and M. Mao, "Assessment of two turbulence models and some compressibility corrections for hypersonic compression corners by high-order difference schemes," *Chinese J. Aeronaut.*, vol. 25, no. 1, pp. 25–32, 2012, doi: 10.1016/S1000-9361(11)60358-0.

[8] A. Kshitij, S. A. Prince, J. L. Stollery, and F. D. L. P. Ricón, "A simple method for drag estimation for wedge-like fairings in hypersonic flow," *Aeronaut. J.*, vol. 125, no. 1288, pp. 968–987, 2021, doi: 10.1017/aer.2021.20.

[9] J. Hao, C. Y. Wen, and J. Wang, "Numerical investigation of hypervelocity shock-wave/boundary-layer interactions over a double-wedge configuration," *Int. J. Heat Mass Transf.*, vol. 138, pp. 277–292, 2019, doi: 10.1016/j.ijheatmasstransfer.2019.04.062.

[10] C. Aliaga, K. Guan, J. Selvanayagam, J. Stokes, V. Viti, and F. Menter, "Hypersonic applications of the laminarturbulent transition SST model in ANSYS fluent," *Aiaa Aviat. 2020 Forum*, vol. 1 PartF, pp. 1–16, 2020, doi: 10.2514/6.2020-3290.

[11] M. MacLean, T. Wadhams, M. Holden, and H. Johnson, "Ground test studies of the HIFiRE-1 transition experiment Part 2: Computational analysis," *J. Spacecr. Rockets*, vol. 45, no. 6, pp. 1149–1164, 2008, doi: 10.2514/1.37693.

[12] T. P. Wadhams, E. Mundy, M. G. MacLean, and M. S. Holden, "Ground test studies of the HIFiRE-1 transition experiment part 1: Experimental results," *J. Spacecr. Rockets*, vol. 45, no. 6, pp. 1134–1148, 2008, doi: 10.2514/1.38338.

[13] J. G. Marvin, J. L. Brown, and P. A. Gnoffo, "Experimental Database with Baseline CFD Solutions: 2-D and Axisymmetric Hypersonic Shock-Wave/Turbulent-Boundary-Layer Interactions," *Nasa/Tm–2013–216604*, no. November, pp. 1–123, 2013.

[14] H.-T. Experiment and M. Holden, "A Computational Analysis of Ground Test Studies of the," no. January, pp. 1–20, 2008.

[15] J. Hao, J. Wang, and C. Lee, "Numerical simulation of high-enthalpy hollow-cylinder/flare flows," *AIAA J.*, vol. 56, no. 8, pp. 3337–3341, 2018, doi: 10.2514/1.J056643.

[16] B. John and V. Kulkarni, "Effect of leading edge bluntness on the interaction of ramp induced shock wave with laminar boundary layer at hypersonic speed," *Comput. Fluids*, vol. 96, pp. 177–190, 2014, doi: 10.1016/j.compfluid.2014.03.004.

[17] D. Ninni, F. Bonelli, G. Colonna, and G. Pascazio, "Unsteady behavior and thermochemical non equilibrium effects in hypersonic double-wedge flows," *Acta Astronaut.*, vol. 191, no. June 2021, pp. 178–192, 2022, doi: 10.1016/j.actaastro.2021.10.040.

[18] M. R. Youssefi and D. Knight, "Assessment of CFD capability for hypersonic shock wave laminar boundary layer interactions," *Aerospace*, vol. 4, no. 2, 2017, doi: 10.3390/aerospace4020025.

[19] D. Knight *et al.*, "Assessment of CFD capability for prediction of hypersonic shock interactions," *Prog. Aerosp. Sci.*, vol. 48–49, pp. 8–26, 2012, doi: 10.1016/j.paerosci.2011.10.001.

[20] G. Tchuen, Y. Burtschell, and D. E. Zeitoun, "Numerical study of the interaction of type IVr around a double-wedge in hypersonic flow," *Comput. Fluids*, vol. 50, no. 1, pp. 147–154, 2011, doi: 10.1016/j.compfluid.2011.07.002.

[21] Z. Sun, T. Gan, and Y. Wu, "Shock-wave/boundary-layer interactions at compression ramps studied by high-speed schlieren," *AIAA J.*, vol. 58, no. 4, pp. 1681–1688, 2020, doi: 10.2514/1.J058257.

[22] A. B. Oliver, R. P. Lillard, G. A. Blaisdell, and A. S. Lyrintzis, "Effects of three-dimensionality in turbulent compression ramp shock-boundary layer interaction computations," *46th AIAA Aerosp. Sci. Meet. Exhib.*, no. January, 2008, doi: 10.2514/6.2008-720.

[23] A. Pandey, K. M. Casper, R. Spillers, M. Soehnel, and S. Spitzer, "Hypersonic shock wave–boundary-layer interaction on the control surface of a slender cone," *AIAA Scitech 2020 Forum*, vol. 1 PartF, no. January, 2020, doi: 10.2514/6.2020-0815.

[24] C. L. Running, T. J. Juliano, J. S. Jewell, M. P. Borg, and R. L. Kimmel, "Hypersonic shock-wave/boundary-layer

interactions on a cone/flare," *Exp. Therm. Fluid Sci.*, vol. 109, no. September, p. 109911, 2019, doi: 10.1016/j.expthermflusci.2019.109911.

[25] P. Raje and K. Sinha, "Anisotropic SST turbulence model for shock-boundary layer interaction," *Comput. Fluids*, vol. 228, no. June, p. 105072, 2021, doi: 10.1016/j.compfluid.2021.105072.

[26] W. Sutherland, " LII. The viscosity of gases and molecular force ," *London, Edinburgh, Dublin Philos. Mag. J. Sci.*, vol. 36, no. 223, pp. 507–531, 1893, doi: 10.1080/14786449308620508.

[27] F. Hypersonic, "Unsteady Separation in Interaction Flow eld," vol. 39, no. 3, pp. 467–470, 2002.

[28] O. Tumuklu, D. A. Levin, and V. Theofilis, "Effects of reynolds number on laminar boundary layer shock-interaction hypersonic flows on a double cone," *2018 Fluid Dyn. Conf.*, pp. 1–21, 2018, doi: 10.2514/6.2018-4032.

[29] A. S. Durna, M. E. H. Ali Barada, and B. Celik, "Shock interaction mechanisms on a double wedge at Mach 7," *Phys. Fluids*, vol. 28, no. 9, 2016, doi: 10.1063/1.4961571.

[30] A. B. Swantek and J. M. Austin, "Heat transfer on a double wedge geometry in hypervelocity air and nitrogen flows," *50th AIAA Aerosp. Sci. Meet. Incl. New Horizons Forum Aerosp. Expo.*, no. January, pp. 1–12, 2012, doi: 10.2514/6.2012-284.

[31] T. D. Canonsburg, "ANSYS Fluent Theory Guide," *ANSYS Inc., USA*, vol. 15317, no. November, p. 814, 2013, [Online]. Available: http://www.afs.enea.it/project/neptunius/docs/fluent/html/th/main_pre.htm.

[32] C. Zhang, J. Xu, L. Gao, and G. Gao, "Studies of compression corner flowfields using three turbulent models," *Procedia Eng.*, vol. 31, pp. 762–768, 2012, doi: 10.1016/j.proeng.2012.01.1099.